Journal of Applied Geophysics 98 (2013) 254–264

Contents lists available at ScienceDirect

Journal of Applied Geophysics

journal homepage: www.elsevier.com/locate/jappgeo

Integration of crosswell seismic data for simulating porosity in a heterogeneous carbonate aquifer

Xavier Emery [a,b,*], Jorge Parra [c]

[a] Department of Mining Engineering, University of Chile, Avenida Tupper 2069, Santiago, Chile
[b] Advanced Mining Technology Center, University of Chile, Avenida Beauchef 850, Santiago, Chile
[c] Division of Applied Physics, Southwest Research Institute, San Antonio, TX, USA

ARTICLE INFO

Article history:
Received 14 June 2013
Accepted 13 September 2013
Available online 20 September 2013

Keywords:
Geological heterogeneity
Data integration
Geostatistical simulation
Non-stationary modeling
Local anamorphosis
Crosswell reflection

ABSTRACT

A challenge for the geostatistical simulation of subsurface properties in mining, petroleum and groundwater applications is the integration of well logs and seismic measurements, which can provide information on geological heterogeneities at a wide range of scales. This paper presents a case study conducted at the Port Mayaca aquifer, located in western Martin County, Florida, in which it is of interest to simulate porosity, based on porosity logs at two wells and high-resolution crosswell seismic measurements of P-wave impedance. To this end, porosity and impedance are transformed into cross-correlated Gaussian random fields, using local transformations. The model parameters (transformation functions, mean values and correlation structure of the transformed fields) are inferred and checked against the data. Multiple realizations of porosity can then be constructed conditionally to the impedance information in the interwell region, which allow identifying one low-porosity structure and two to three flow units that connect the two wells, mapping heterogeneities within these units and visually assessing fluid paths in the aquifer. In particular, the results suggest that the paths in the lower flow units, formed by a network of heterogeneous conduits, are not as smooth as in the upper flow unit.

1. Introduction

Seismic measurements and well logs are commonly used to characterize rock properties and geological heterogeneities in the subsurface. Examples of applications include mining and petroleum exploration, in which it is of interest to describe heterogeneous ore deposits and reservoirs at multiple scales. These applications are usually focused on understanding the nature of the heterogeneity and on improving algorithms to produce reliable deposit or reservoir models. Such models, which integrate cores, well logs, seismic and production data are used to identify mineral resources, to locate unswept oil in reservoirs under waterflood, or to forecast oil reservoir performance (Ikelle and Amundsen, 2005; Jennings et al., 2000; Kerans et al., 1994; Malehmir et al., 2012).

In groundwater applications, the integration of seismic data and well logs can provide information at a wide range of scales in order to predict the rock physical properties and the geological heterogeneities of an aquifer, which is essential for flow transport modeling and for designing cost-effective aquifer remediation and water management procedures (Dafflon et al., 2009). The geophysical attributes capture the geological structures and their physical properties, allowing mapping and characterizing flow units at large well separations to minimize the number of wells, thus avoiding unnecessary disruptions of the environment. Although a combination of surface reflection seismic and well log data can help to delineate large scale heterogeneities and structural features in aquifers (Parra et al., 2006), it is also important to conduct high-resolution crosswell seismic measurements to predict rock physical properties such as permeability and porosity at local scales in the region between wells.

To relate the geological units or the lithology of an aquifer to its petrophysics, it is imperative to have a standard suite of well logs (e.g., porosity, permeability, resistivity, gamma ray). For limestone aquifers, formation micro-imager (FMI) logs are recommended to provide the microstructure characteristics of the formation at the well location. In carbonate aquifers, the FMI logs allow estimation of primary (matrix) and secondary porosities. Processing the FMI logs also yields vuggy and crack porosity logs. The primary or matrix porosity can contain interconnected pores to create a water flow path, and the secondary porosity can be formed by isolated or connected vugs. Connected vugs in the matrix form good water conduits, while isolated vugs form low-permeability flow paths (Kazatchenko et al., 2006). Cores and well logs provide relevant information about the rock-fabric facies, which is used to describe heterogeneities and to predict fluid paths in the aquifer at the well scale. By using porosity and permeability data captured

* Corresponding author at: Department of Mining Engineering, University of Chile, Avenida Tupper 2069, Santiago, Chile. Tel.: +56 2 2978 4498; fax: +56 2 2978 4985.
E-mail address: xemery@ing.uchile.cl (X. Emery).

0926-9851/$ – see front matter © 2013 Elsevier B.V. All rights reserved.
http://dx.doi.org/10.1016/j.jappgeo.2013.09.004

by seismic waves, as well as seismic data acquired between wells, one can relate the seismic attributes with petrophysical data at the well scale to characterize the aquifer between wells. The most common attributes extracted from seismic data are P-wave velocity, impedance and attenuation.

Geostatistical techniques such as kriging and cokriging have been widely used to integrate seismic data with well log data (Doyen, 1988; Dubrule, 2003; Parra and Emery, 2013). These techniques allow mapping or delineating flow units but do not provide information about pore structure variability (or heterogeneities) within these units. Although the relationship between total porosity and the lithological units at the well scale are generally understood, there is a need to identify and to visualize the distribution of small-scale heterogeneities in aquifers at the interwell region, which can be achieved by means of stochastic simulation (Belina et al., 2009; Dafflon and Barrash, 2012; Dafflon et al., 2009; Dubreuil-Boisclair et al., 2011).

In this paper, we describe a work conducted at the Port Mayaca aquifer in western Martin County, Florida, in which stochastic simulation is used to visualize the small-scale aquifer heterogeneity. Our study incorporates previous well examinations at the site (Parra et al., 2009), in which tight limestone features are clearly observed at several FMI depths. These features are correlated with elemental log analysis (ELAN, Schlumberger propriety software) porosity logs. Several thinner resistive streaks shown in the FMI logs are not resolved by the ELAN porosity logs, but lower porosity in a permeability barrier interval (Bennett and Recrenwald, 2002). Between these resistive streaks are thin, conductive limestone zones corresponding to isolated secondary porosity.

For the current study, ELAN porosity logs are integrated with crosswell P-wave seismic impedance. We selected a high water production zone in the interwell region, and ELAN porosity logs from Port Mayaca wells MF-37 and EXPM-1 were used to acquire the crosswell data. Basic statistics of the data are provided in Table 1. The ELAN porosity, available along the wells with a resolution of 0.15 m (0.5 ft), represents the lithological variability of the aquifer at the well scale, while P-wave impedance data are obtained by inverting crosswell seismic reflection measurements, with a resolution of 3.05 m (10 ft) in the east–west direction and 0.61 m (2 ft) in depth (Parra et al., 2006, 2009).

2. Joint modeling of ELAN porosity and P-wave impedance

2.1. Basic hypotheses

In the following, we will work in the two-dimensional space formed by the cross-section between wells MF-37 and EXPM-1. A generic location in this space will be represented by a vector $\mathbf{x} = (x_1,x_2)$ indicating the east and depth coordinates. ELAN porosity and P-wave impedance are viewed as realizations of two cross-correlated spatial random fields, which will be denoted by Z_1 and Z_2, respectively.

Modeling the joint distribution of these random fields faces two main difficulties:

1) ELAN porosity is known only at wells MF-37 and EXPM-1, in the edges of the region of interest, so that there is little direct information about the spatial continuity of this variable along the east–west direction.

Table 1
Statistics of ELAN porosity (dimensionless) at wells MF-37 and EXPM-1 and P-wave impedance ((g/cm^3) (ft/s)) in the interwell region.

	ELAN porosity	P-wave impedance
Number of data	1070	17,145
Minimum	0.1946	7253.2
Maximum	0.4896	23,824.6
Mean	0.3921	15,943.9
Standard deviation	0.0435	2119.9

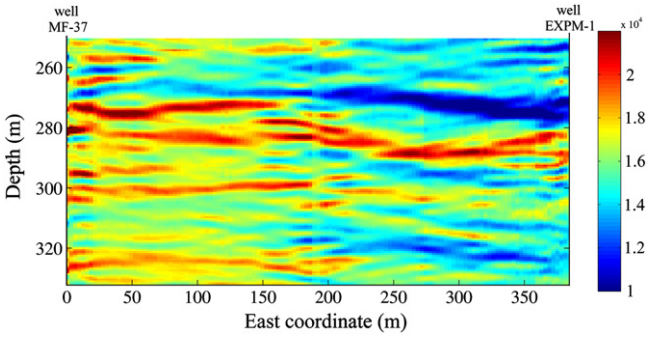

Fig. 1. Map of P-wave impedance in the interwell region.

2) The distributions of ELAN porosity and P-wave impedance are likely not to be the same everywhere in the interwell region. In particular, the map of P-wave impedance (Fig. 1) and the scatter plots of P-wave impedance along each coordinate axis (Fig. 2) suggest the presence of a systematic trend along the east coordinate (with greater impedance values to the west and lower values to the east), whereas no obvious trend is perceptible along the vertical direction (well direction). One therefore expects the random fields associated with ELAN porosity and P-wave impedance to be non-stationary, with distributions that vary along the east–west direction.

The key idea of the model that will be proposed is to transform the ELAN porosity and P-wave impedance into two cross-correlated Gaussian random fields. The non-stationarity of ELAN porosity and P-wave impedance will be modeled through the use of local transformations, which vary along the east–west direction, while the transformed (Gaussian) random fields will be considered as stationary (i.e., with distributions invariant under a translation in space), in order to ease the inference of their spatial correlation structure and to achieve their simulation subject to conditioning data. In the following subsections, we will determine the local transformations at the well locations and in the interwell region, then we will turn to the modeling of the spatial correlation structure.

2.2. Transforming ELAN porosity data into normally distributed data

Let $\mathbf{x} = (x_1,x_2)$ be a location in the interwell region. It is assumed that the ELAN porosity at this location, $Z_1(\mathbf{x})$, is the transform of a standard Gaussian random variable, $Y_1(\mathbf{x})$:

$$Z_1(\mathbf{x}) = \phi_{\mathbf{x}}(Y_1(\mathbf{x})), \tag{1}$$

where $\phi_{\mathbf{x}}$ is a non-decreasing function called Gaussian anamorphosis (Chilès and Delfiner, 2012). This function characterizes the distribution of ELAN porosity at location $\mathbf{x}$. It depends on $\mathbf{x}$ or, more precisely, on its first coordinate x_1, because of the assumed non-stationarity along the east–west direction. To model the anamorphosis, let us consider its expansion into Hermite polynomials (Rivoirard, 1994; Wackernagel, 2003):

$$\forall y \in \mathbb{R},\ \phi_{\mathbf{x}}(y) = \sum_{p=0}^{+\infty} \phi_p(x_1) H_p(y), \tag{2}$$

where $\{\phi_p(x_1):\ p \in \mathbb{N}\}$ are real coefficients (functions of x_1) and $\{H_p:\ p \in \mathbb{N}\}$ are the normalized Hermite polynomials. These polynomials are defined as:

$$H_p(y) = \frac{1}{\sqrt{p!}\,g(y)} \frac{d^p g(y)}{dy^p}, \tag{3}$$

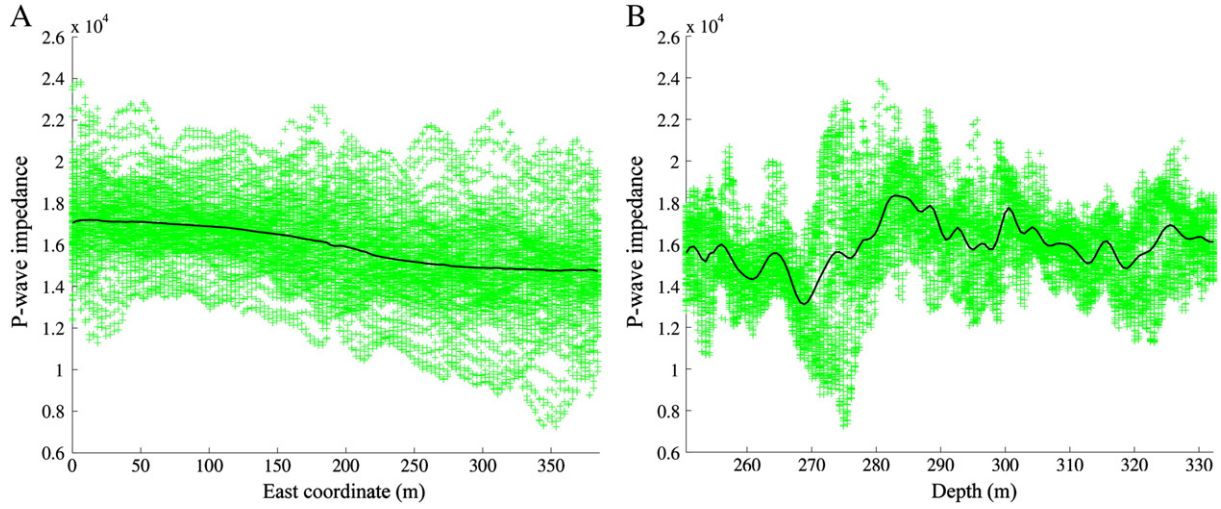

Fig. 2. Scatter plot of P-wave impedance versus A) east coordinate and B) depth. The conditional means are superimposed on each plot (solid lines).

where g stands for the standard Gaussian probability density function. Given an anamorphosis function $\phi_{\mathbf{x}}$, the decomposition into Hermite polynomials is unique, so that $\phi_{\mathbf{x}}$ is fully characterized by the set of coefficients $\{\phi_p(x_1): p \in \mathbb{N}\}$.

One can experimentally estimate $\phi_{\mathbf{x}}$ and its associated Hermite coefficients for coordinates $x_1 = 0$ m and $x_1 = 382.5$ m (1255 ft), corresponding to the locations of wells MF-37 and EXPM-1. As an illustration, the first two coefficients are given in Table 2. Note that the coefficient of order 0 is nothing more than the mean value of ELAN porosity. This is explained because $H_0(y) = 1$ and, for $p > 0$, the expected value of $H_p(Y)$ is zero when Y is a standard Gaussian random variable (Rivoirard, 1994).

2.3. Modeling the distributions of ELAN porosity and P-wave impedance in the interwell region

Although the anamorphosis functions of ELAN porosity are not the same at wells MF-37 and EXPM-1, their difference mainly concerns the first two coefficients $\phi_0(x_1)$ and $\phi_1(x_1)$, associated with the Hermite polynomials of degrees 0 and 1. This is corroborated by plotting this difference, which appears to be almost linear, except in the tail of negative Gaussian values corresponding to low porosity values (this may be explained because, for both wells, the porosity distribution is negatively skewed and its lower tail is poorly known due to the small amount of data) (Fig. 3).

Based on this observation, we will assume that, for $p \geq 2$, the coefficient associated with the Hermite polynomial of degree p, $\phi_p(x_1)$, does not vary in the interwell region, i.e., it actually does not depend on coordinate x_1. The ELAN porosity anamorphosis (Eq. (2)) can therefore be expanded as:

$$\forall y \in \mathbb{R},\ \phi_{\mathbf{x}}(y) = \phi_0(x_1) + \phi_1(x_1)H_1(y) + \sum_{p=2}^{+\infty} \phi_p H_p(y). \tag{4}$$

Each constant coefficient ϕ_p with $p \geq 2$ can be experimentally estimated by averaging the ϕ_p coefficients found for wells MF-37 and EXPM-1. To complete the determination of the ELAN porosity distribution in the interwell region, it therefore remains to determine the spatially-varying coefficients $\phi_0(x_1)$ and $\phi_1(x_1)$. To this end, we will use the information of the covariate (P-wave impedance).

Table 2
First coefficients of the ELAN porosity anamorphosis at wells MF-37 and EXPM-1.

Order	Coefficient for well MF-37	Coefficient for well EXPM-1
0	0.3760	0.4082
1	−0.0371	−0.0402

As for ELAN porosity, let us assume that the P-wave impedance at location $\mathbf{x} = (x_1,x_2)$, denoted by $Z_2(\mathbf{x})$, is the transform of a standard Gaussian random variable, $Y_2(\mathbf{x})$:

$$Z_2(\mathbf{x}) = \varphi_{\mathbf{x}}(Y_2(\mathbf{x})), \tag{5}$$

with

$$\forall y \in \mathbb{R},\ \varphi_{\mathbf{x}}(y) = \sum_{p=0}^{+\infty} \varphi_p(x_1)H_p(y), \tag{6}$$

for a unique set of real coefficients $\{\varphi_p(x_1): p \in \mathbb{N}\}$.

Since P-wave impedance is exhaustively known in the interwell region, the anamorphosis function $\varphi_{\mathbf{x}}$ or, equivalently, its Hermite coefficients $\{\varphi_p(x_1): p \in \mathbb{N}\}$ can be estimated experimentally for any coordinate x_1. It is interesting to note that the coefficients $\varphi_0(x_1)$ and $\varphi_1(x_1)$ vary to a great extent with the coordinate, whereas the coefficients of greater orders have a smaller range of variation and could therefore be considered as constant in the interwell region (Fig. 4), which is precisely the same assumption made for ELAN porosity:

$$\forall y \in \mathbb{R},\ \varphi_{\mathbf{x}}(y) = \varphi_0(x_1) + \varphi_1(x_1)H_1(y) + \sum_{p=2}^{+\infty} \varphi_p H_p(y). \tag{7}$$

For the particular coordinates $x_1 = 0$ m and $x_1 = 382.5$ m, corresponding to the locations of wells MF-37 and EXPM-1, the first two coefficients are indicated in Table 3.

To go further and to achieve the modeling of the ELAN porosity distribution, the idea is to relate the first two ELAN porosity coefficients, $\phi_0(x_1)$ and $\phi_1(x_1)$, with the first two P-wave impedance coefficients, $\varphi_0(x_1)$ and $\varphi_1(x_1)$. On the one hand, the coefficients of order 0 represent the mean values of the raw (untransformed) variables (Rivoirard, 1994). Furthermore, a look at the scatter plot between the ELAN porosity and P-wave impedance at the well locations (Fig. 5) indicates a linear relationship between these two variables. In order to fit the mean values observed at the well locations (Tables 2 and 3), this relationship can be modeled in the following way (Parra and Emery, 2013):

$$\text{mean porosity} + 0.000014 \times \text{mean impedance} = 0.615, \tag{8}$$

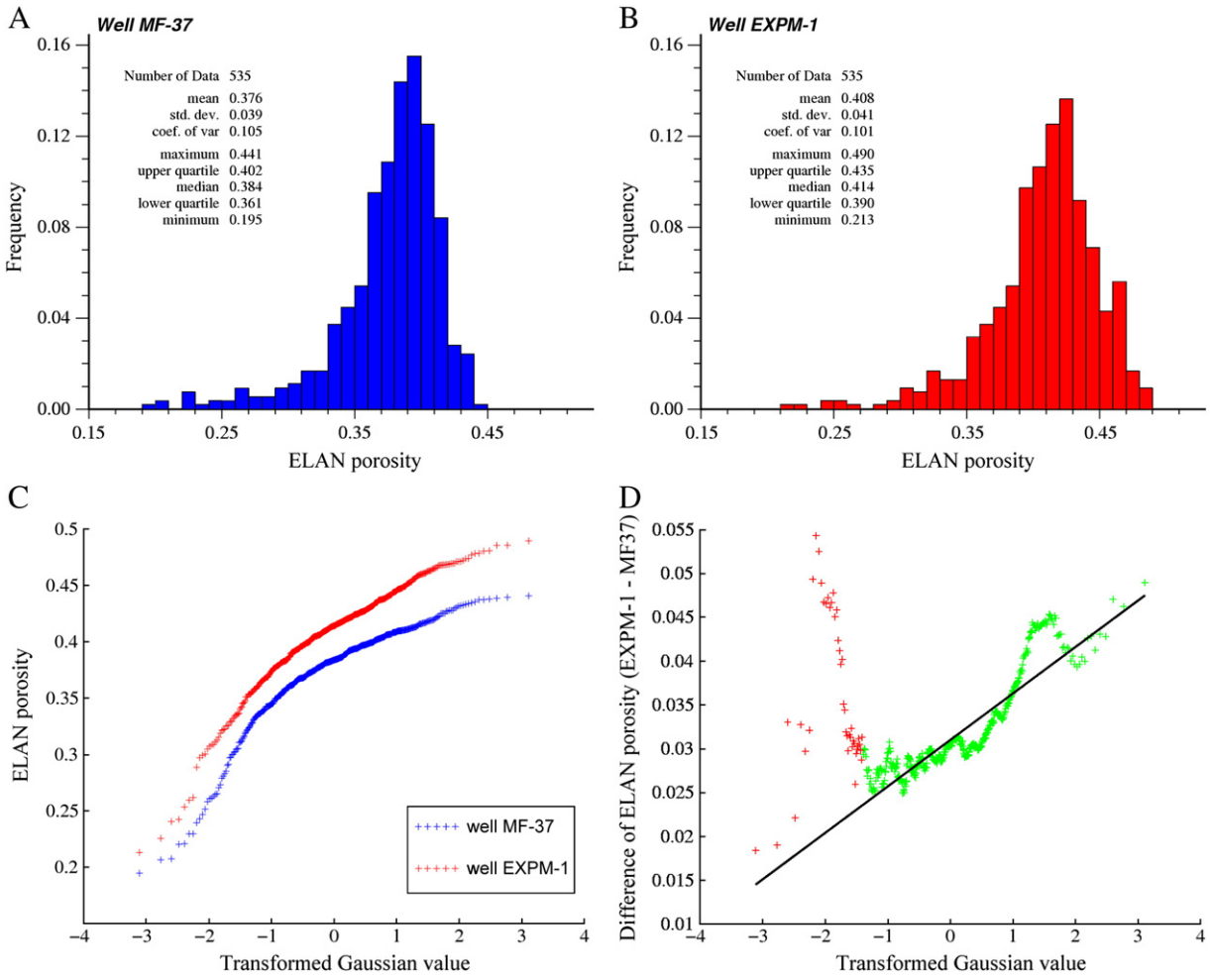

Fig. 3. A) ELAN porosity distribution at well MF-37, B) ELAN porosity distribution at well EXPM-1, C) Gaussian anamorphoses for ELAN porosity at wells MF-37 and EXPM-1, D) Difference between both anamorphoses and its approximation by a straight line ($R^2 = 0.80$ if one omits the subset of 43 points painted in red and only accounts for the 492 points painted in green).

i.e., in terms of zero-order coefficients:

$$\phi_0(x_1) + 0.000014\varphi_0(x_1) = 0.615. \quad (9)$$

On the other hand, if one calculates the ratios between the first coefficients of ELAN porosity and P-wave impedance at the well locations (Tables 2 and 3), it is noticeable that approximately the same value is obtained for the two wells:

$$\frac{\phi_1(0)}{\varphi_1(0)} = 0.0000192 \text{ and } \frac{\phi_1(382.5)}{\varphi_1(382.5)} = 0.0000188. \quad (10)$$

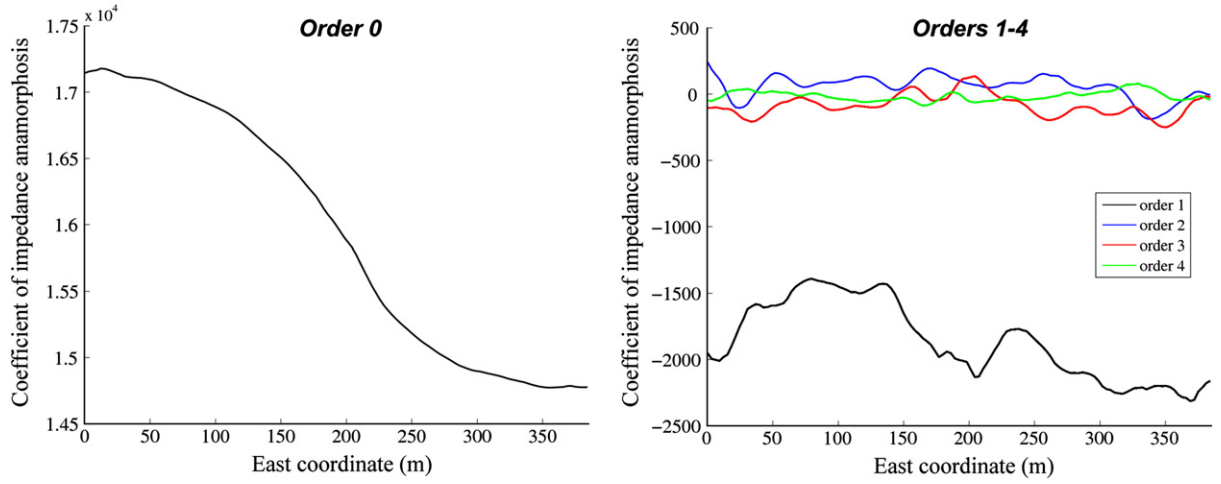

Fig. 4. Evolution of the first five coefficients of the P-wave impedance anamorphosis, as a function of the east coordinate.

Table 3
First coefficients of the P-wave impedance anamorphosis at wells MF-37 and EXPM-1.

Order	Coefficient for well MF-37	Coefficient for well EXPM-1
0	17,074	14,777
1	−1925.2	−2133.6

Accordingly, we will assume that this ratio between coefficients remains the same in the interwell region and impose, for any coordinate x_1:

$$\phi_1(x_1) = 0.000019\varphi_1(x_1). \tag{11}$$

In terms of the raw variables (ELAN porosity and P-wave impedance), this relationship will allow Eq. (8) to remain valid, at a first-order approximation, even if the distributions of the transformed variables deviate from a standard Gaussian distribution, as will be explained in Section 2.6.

2.4. Spatial modeling via Gaussian random fields

For simulation, we will further assume that the transformed porosity and impedance fields are stationary Gaussian random fields, i.e., their finite-dimensional distributions are multivariate normal and are invariant under a translation in space (Chilès and Delfiner, 2012). To corroborate these assumptions, let us first compare the experimental variograms of the transformed porosity calculated along the vertical direction, for both wells (MF-37 and EXPM-1): these variograms turn out to be very similar (Fig. 6), which agrees with the stationarity assumption. In order to check multivariate normality, let us consider spatial continuity measures known as "variograms of order ω" (Matheron, 1989):

$$\begin{cases} \gamma_1^{(\omega)}(\mathbf{h}) = \frac{1}{2}E\{|Y_1(\mathbf{x}+\mathbf{h}) - Y_1(\mathbf{x})|^{\omega}\} \\ \gamma_2^{(\omega)}(\mathbf{h}) = \frac{1}{2}E\{|Y_2(\mathbf{x}+\mathbf{h}) - Y_2(\mathbf{x})|^{\omega}\} \end{cases}, \tag{12}$$

where $E\{.\}$ stands for the mathematical expectation, $\mathbf{h}$ for a separation vector and ω for a positive real value. Experimentally, these variograms of order ω can be estimated by replacing the expectation by an average over the pairs of data with locations separated by $\mathbf{h}$ (Chilès and Delfiner, 2012). The case $\omega = 2$ corresponds to the traditional variogram. In the case of stationary Gaussian random fields, the following identities hold (Emery, 2005):

$$\gamma_1^{(\omega)}(\mathbf{h}) = \frac{2^{\omega-1}}{\sqrt{\pi}}\Gamma\left(\frac{\omega+1}{2}\right)\left[\gamma_1^{(2)}(\mathbf{h})\right]^{\omega/2} \tag{13}$$

$$\gamma_2^{(\omega)}(\mathbf{h}) = \frac{2^{\omega-1}}{\sqrt{\pi}}\Gamma\left(\frac{\omega+1}{2}\right)\left[\gamma_2^{(2)}(\mathbf{h})\right]^{\omega/2}. \tag{14}$$

Eqs. (13) and (14) indicate that, in log–log coordinates, the points representing the variogram of order ω as a function of the traditional variogram should be aligned with slope ω/2. As shown in Fig. 7 for $\omega = 1$ and $\omega = 0.5$, this property is well satisfied with the Gaussian transforms of ELAN porosity and P-wave impedance data, corroborating that the transformed fields can be modeled as stationary Gaussian random fields.

2.5. Modeling the spatial correlation structure

Gaussian random fields are characterized by their mean values and their joint spatial correlation structure, which can be represented by direct and cross covariances or by direct and cross variograms (Wackernagel, 2003). For ELAN porosity (Gaussian random field Y_1), the variogram can be calculated experimentally along the vertical direction (well direction) for lag distances that are multiples of 0.15 m and along the east–west direction for a single lag distance of 382.5 m, corresponding to the distance that separates the two wells. For P-wave impedance (Gaussian random field Y_2), the variogram can be calculated along the vertical direction for lag distances that are multiples of 0.61 m and along the east–west direction for lag distances that are multiples of 3.05 m, corresponding to the grid mesh at which P-wave impedance is available. As for the cross variogram, it can be calculated along the vertical direction for lag distances that are multiples of 0.61 m and along the east–west direction for a single lag distance of 382.5 m. These experimental variograms exhibit a dampened periodic behavior along the vertical direction, but not along the east–west direction, and a finite sill in both directions (Fig. 8).

The fitting of variogram models is complicated by the fact that the ELAN porosity variogram and the cross variogram are mostly unknown along the east–west direction. However, it is observed that the direct and cross variograms have similar shapes along the vertical direction, except for small distances (the ELAN porosity variogram grows faster

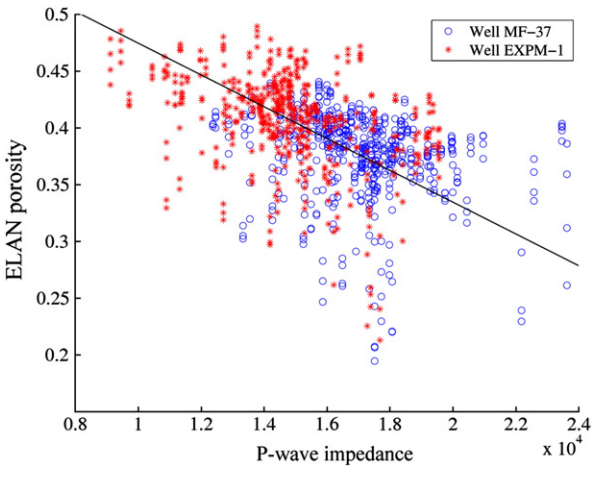

Fig. 5. Scatter plot of P-wave impedance versus ELAN porosity at well locations. The modeled linear relationship (Eq. (8)) is superimposed.

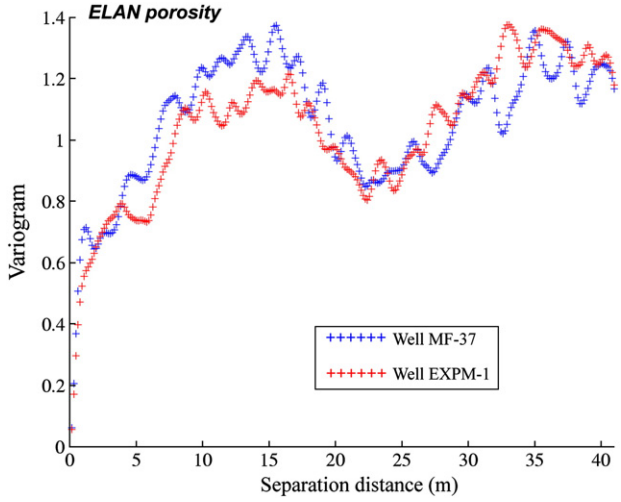

Fig. 6. Experimental variograms of the Gaussian transform of ELAN porosity, calculated along the vertical direction.

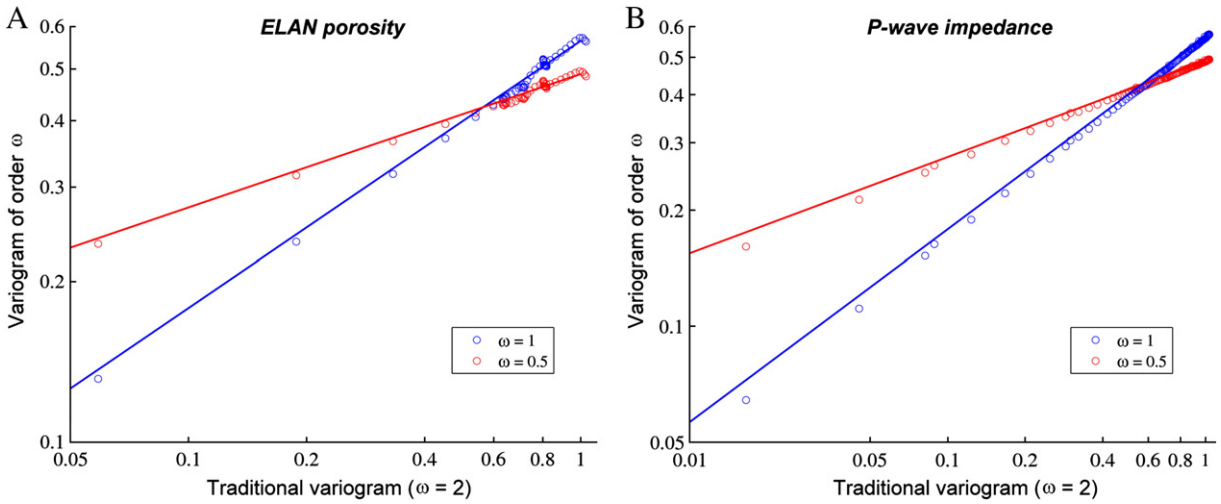

Fig. 7. Variograms of order 1 (blue) and of order 0.5 (red) as a function of the traditional variogram, for the Gaussian transforms of ELAN porosity (A) and P-wave impedance (B). Circles: experimental variograms calculated along the vertical and east–west directions. Solid lines: theoretical models (Eqs. (13)–(14)) under an assumption of multivariate normality.

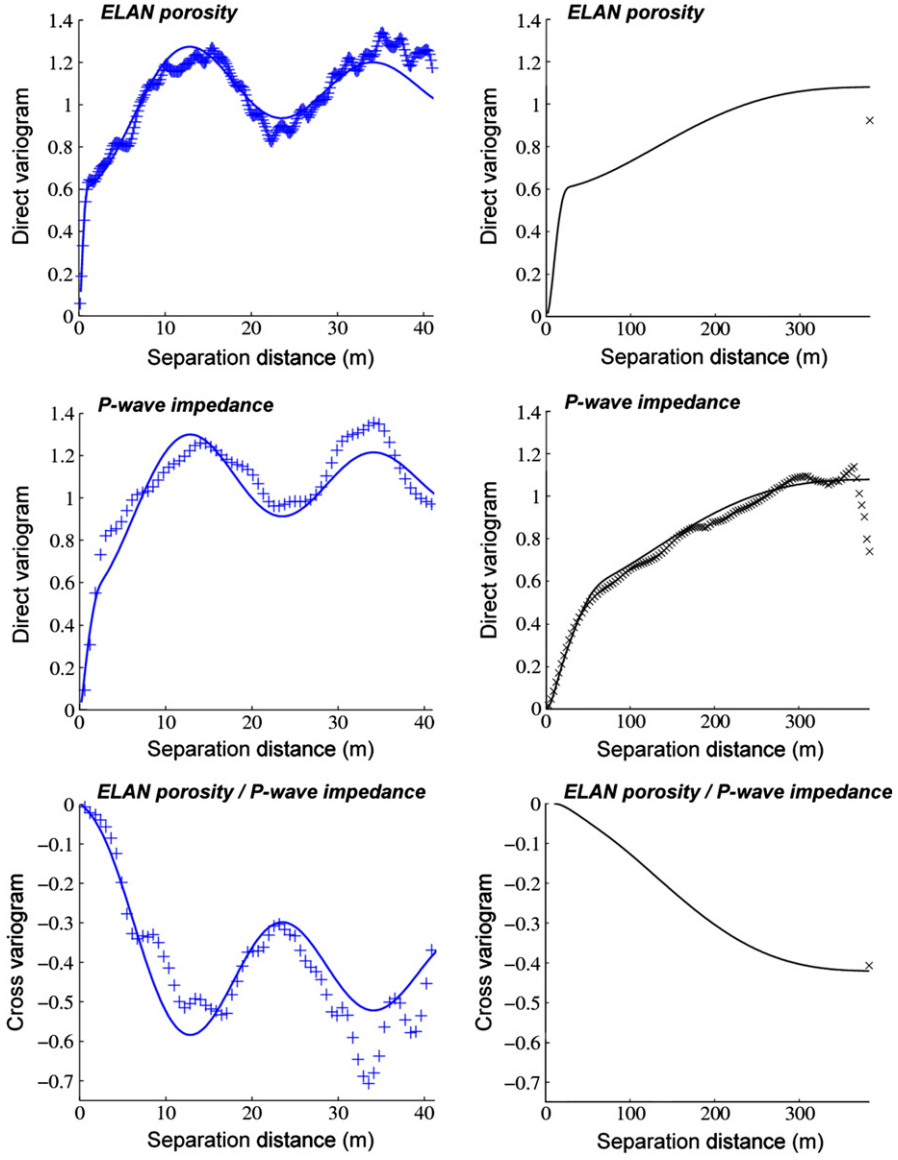

Fig. 8. Direct and cross variograms for the Gaussian transforms of ELAN porosity and P-wave impedance, along the vertical direction (left) and east–west direction (right). Crosses: experimental variograms; solid lines: fitted theoretical models.

than the P-wave impedance variogram, while the cross variogram does not exhibit a small-scale structure). A fit can be undertaken by using a linear coregionalization model (Wackernagel, 2003), which consists in modeling all the variograms by the same set of basic nested structures. Specifically, three basic structures are considered:

- a cubic structure with ranges 30.5 m (east–west) and 1.22 m (vertical);
- a cubic structure with ranges 85.3 m (east–west) and 3.05 m (vertical);
- a separable structure, obtained by multiplying a dampened periodic covariance along the vertical direction (a J-Bessel covariance function of order 0 and scale factor 3.35 m) and a monotonic covariance along the east–west direction (cubic with range 426.7 m).

The ranges and scale factors along the vertical directions have been chosen in order to fit all the direct and cross variograms, while the ranges along the east–west direction have been chosen in order to fit the direct variogram of P-wave impedance: the separable structure models the large-scale behavior and the first two cubic structures model the small-scale behavior. Although the first cubic structure has a smaller contribution than the second one to the variogram of P-wave impedance, this contribution is not negligible, so that its range can be reasonably inferred.

The mathematical expression of the above-mentioned basic structures can be found in the specialized literature (Chilès and Delfiner, 2012). The fitting of the sills associated with each structure is performed by using an iterative algorithm (Emery, 2010), which provides the model that minimizes the squared deviations between experimental and fitted variograms. The results are displayed in Fig. 8. Overall, the direct and cross variograms have a similar large-scale behavior, governed by the separable structure, but their small-scale behaviors are different (reflecting different small-scale variability for ELAN porosity and P-wave impedance). The first cubic structure has a larger contribution to the direct variogram of ELAN porosity, while the second cubic structure has a larger contribution to the direct variogram of P-wave impedance. Both structures help to model the variogram increase at small distances, which is faster for ELAN porosity than for P-wave impedance, and have a small contribution to the cross variogram, which is dominated by the separable structure.

2.6. Revisiting the assumption of standard Gaussian distributions

When looking back at the fitted variogram models (Fig. 8), it is seen that the sills of the direct variograms are slightly greater than 1: more precisely, these sills are equal to 1.08 for both ELAN porosity and P-wave impedance. Since the variogram sill coincides with the variance of the random field, this means that the transformed random fields Y_1 and Y_2 do not have a unit variance.

This observation leads us to revisit the assumption that these transformed fields are standard Gaussian, i.e., with zero mean and unit variance. It would actually be more convenient to assume that the mean values and variances may slightly deviate from zero and one, respectively. Relaxing the assumption of zero mean and unit variance has no effect on the variogram analysis stage (Section 2.5) or on the calculation of variograms of order ω (Section 2.4). However the mean values of the Hermite polynomials now differ from zero, so that the anamorphosis coefficients of order 0 do not coincide with the mean values of the raw variables any more (Rivoirard, 1994). Accordingly, the relationship given in Eq. (9) may not be equivalent to the desired relationship between the mean values of ELAN porosity and P-wave impedance (Eq. (8)).

To examine whether or not the mean values of ELAN porosity and P-wave impedance are modified in a significant manner, let us come back to the expansions of the anamorphoses into Hermite polynomials (Eqs. (2) and (6)) and consider a first-order approximation:

$$\forall \mathbf{x}=(x_1,x_2),\ \begin{cases} E\{Z_1(\mathbf{x})\}\approx \phi_0(x_1)+\phi_1(x_1)E\{H_1(Y_1(\mathbf{x}))\} \\ E\{Z_2(\mathbf{x})\}\approx \varphi_0(x_1)+\varphi_1(x_1)E\{H_1(Y_2(\mathbf{x}))\} \end{cases}. \tag{15}$$

Since $H_1(y) = -y$ (Eq. (3)), it comes:

$$\forall \mathbf{x}=(x_1,x_2),\ \begin{cases} E\{Z_1(\mathbf{x})\}\approx \phi_0(x_1)-m_1\phi_1(x_1) \\ E\{Z_2(\mathbf{x})\}\approx \varphi_0(x_1)-m_2\varphi_1(x_1) \end{cases}, \tag{16}$$

where m_1 and m_2 are the mean values of $Y_1(\mathbf{x})$ and $Y_2(\mathbf{x})$, assumed constant in space. Accounting for Eqs. (9) and (11), imposed in the anamorphosis modeling stage, one obtains:

$$E\{Z_1(\mathbf{x})\}+0.000014E\{Z_2(\mathbf{x})\}\approx 0.615 -(0.000014m_2+0.000019m_1)\varphi_1(x_1). \tag{17}$$

It is therefore possible to preserve the relationship (Eq. (8)) between the mean ELAN porosity and the mean P-wave impedance, by imposing the following constraint between the mean values of the Gaussian random fields Y_1 and Y_2:

$$m_1=-\frac{0.000014}{0.000019}m_2=-0.737m_2. \tag{18}$$

2.7. Summary of the joint model for ELAN porosity and P-wave impedance

In summary, the distribution of ELAN porosity in the interwell region is modeled through a spatially-varying Gaussian anamorphosis function (Eq. (4)), whose Hermite coefficients of order 0 and 1 are related to that of the P-wave impedance anamorphosis (Eqs. (9) and (11)), while the coefficients of greater orders are constant in space and can be estimated experimentally from the well data. The Gaussian transforms of ELAN porosity and P-wave impedance constitute jointly stationary Gaussian random fields, with means related through Eq. (18) and with a spatial correlation structure given by the direct and cross variograms displayed in Fig. 8. It is interesting to note that the dependence relationship between ELAN porosity and P-wave impedance is twofold: on the one hand, a stochastic dependence modeled by the cross-variogram; on the other hand, a functional dependence modeled by the linear relationship between the mean values (Eq. (8)).

3. Simulation of ELAN porosity

3.1. Non-conditional simulation

Before simulating ELAN porosity conditionally to P-wave impedance data, it is interesting to draw a few non-conditional realizations of these two variables. To this end, the cross-correlated Gaussian random fields Y_1 and Y_2 are cosimulated on the grid on which the P-wave impedance is known, with no conditioning data, by using an adaptation of the turning bands program proposed by Emery (2008). The simulated Gaussian random fields are transformed into ELAN porosity and P-wave impedance fields by applying the modeled anamorphosis functions, which are known through their expansions into Hermite polynomials (Eqs. (4) and (7)).

The non-conditional realizations can be used to qualitatively validate the fitted model. In particular, one can visually check that the spatial continuity of P-wave impedance is adequately reproduced, by comparing the maps of the impedance realizations (Fig. 9) with the true impedance map (Fig. 1).

3.2. Simulation of ELAN porosity conditioned to P-wave impedance data

The realizations of ELAN porosity and P-wave impedance can be made conditional to the known impedance data through a post-

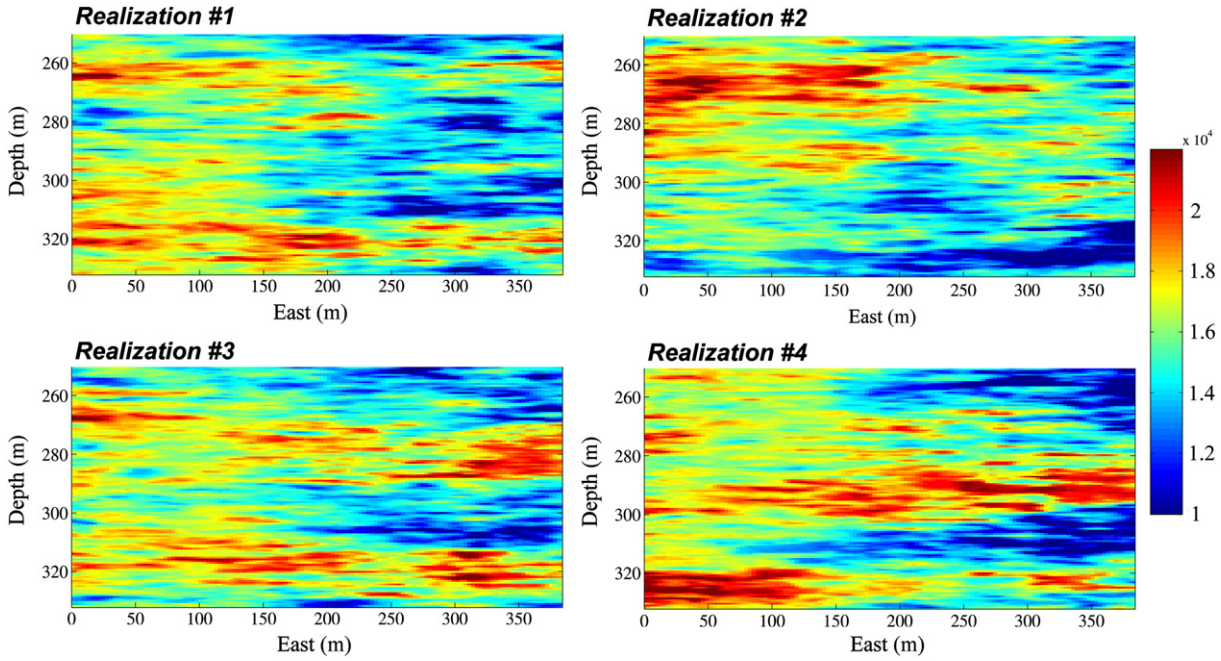

Fig. 9. Maps of non-conditional realizations of P-wave impedance, to compare with Fig. 1.

processing step based on cokriging (Chilès and Delfiner, 2012; De Fouquet, 1994). In the present case, a particular type of cokriging must be used, in order to account for the relationship between the mean values of the underlying Gaussian random fields (Eq. (18)) (Emery, 2012). As an illustration, Fig. 10 presents the maps of four conditional realizations of ELAN porosity in the interwell region (the maps of P-wave impedance realizations are all equal to the map in Fig. 1, as the realizations are conditioned to the impedance data), while Table 4 summarizes the main statistics of these four realizations.

Each conditional realization of ELAN porosity provides an image of the spatial variability of the true unknown values. By comparing Figs. 9 and 10, one observes that the small-scale variability is higher with ELAN porosity than with P-wave impedance. This is explained because the growth of the ELAN porosity variogram at short distances is faster than that of the P-wave impedance variogram (Fig. 8).

The realizations of ELAN porosity suggest the existence of major geological structures in the interwell region. In particular, one can observe a low-porosity structure in the depth interval between 270 m and 300 m, which actually corresponds to a permeability barrier with small-scale lateral porosity zones related to tight limestone features and isolated vugs, an interpretation that is supported by well log data (Parra et al., 2009). The high-porosity structure in the upper part is a flow unit with small lateral variability associated with vuggy porosity; this unit is formed

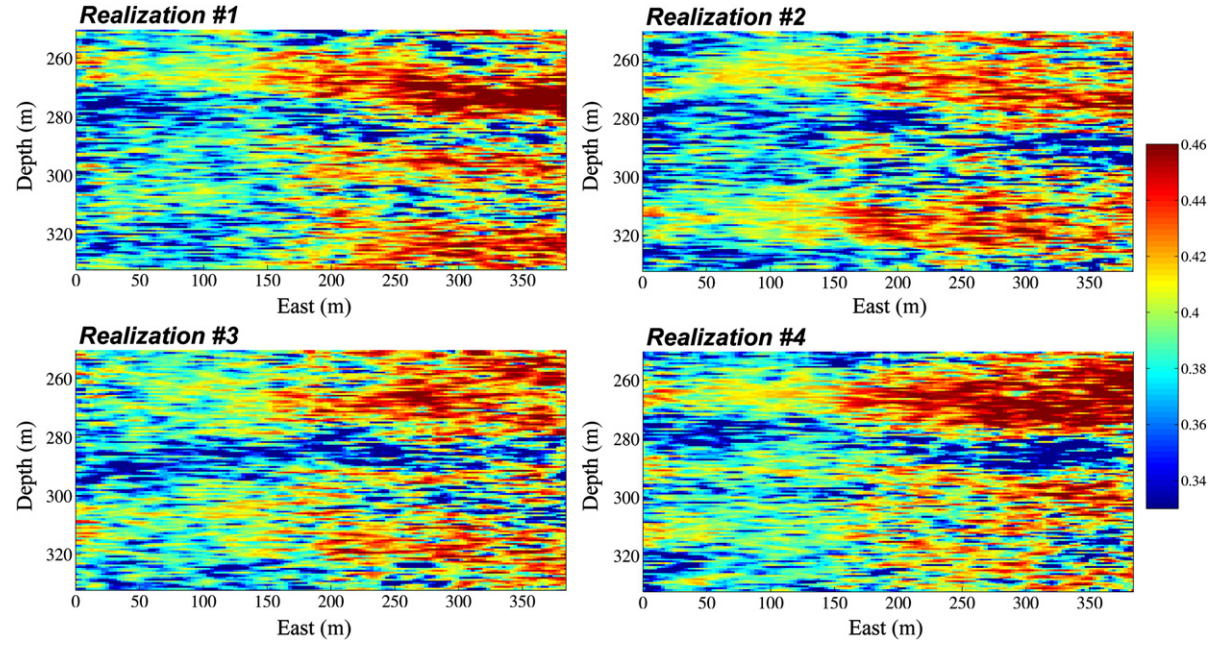

Fig. 10. Maps of conditional realizations of ELAN porosity.

Table 4
Basic statistics of simulated ELAN porosity (realizations 1–4).

Realization	Minimum	Maximum	Mean	Standard deviation	Correlation with impedance
1	0.1915	0.4997	0.3927	0.0405	−0.4764
2	0.1905	0.4953	0.3888	0.0411	−0.4391
3	0.2015	0.4925	0.3902	0.0392	−0.4090
4	0.1985	0.4996	0.3920	0.0433	−0.4644

by large structures that are characterized by interconnected matrix and vugs. In contrast, the structures below the permeability barrier are flow units formed by a network of heterogeneous conduits that are characterized by a combination of lateral interconnected vugs surrounded by tight limestone units. The variability of low porosity tight limestone and the interconnected pores provide a visual assessment of the fluid paths in the aquifer. In the lower flow units, the fluid path is not as smooth as in the upper flow unit.

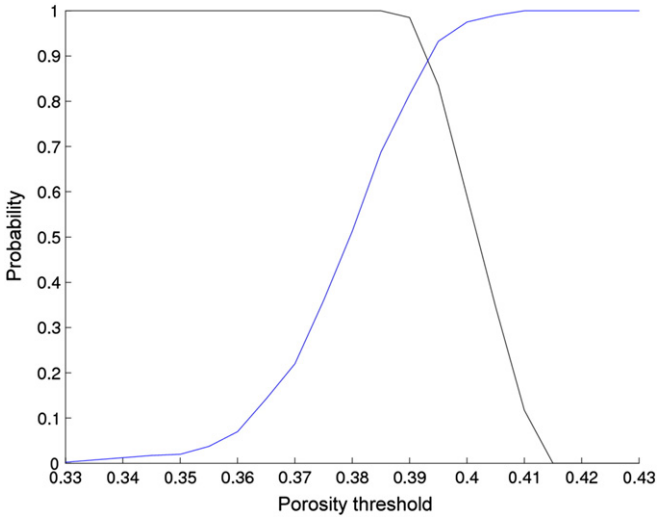

Fig. 12. Probability that a high-porosity structure (decreasing curve) or that a low-porosity structure (increasing curve) connects the two wells. "High" and "low" porosity are defined in relation to a porosity threshold indicated in abscissa.

3.3. Processing the realizations

Several outputs can be calculated from the realizations of ELAN porosity. For instance, Fig. 11 maps the mean and standard deviation of ELAN porosity at each location in the interwell region, as well as the probabilities that the true ELAN porosity is less than 0.40 or 0.38. All these maps have been calculated from a set of 400 conditional realizations. A few artifacts are discernable, especially in the middle of the interwell region (east coordinate close to 190 m). These are caused by artifacts in the P-wave impedance map (Fig. 1), which could have been filtered out prior to the modeling stage. Note that the artifacts are hardly perceptible in the individual realizations (Fig. 10), as they are eclipsed by the small-scale variability of ELAN porosity.

The mean ELAN porosity gives a prediction map similar to what can be obtained by cokriging (Parra and Emery, 2013). The standard deviation measures the uncertainty in the true unknown ELAN porosity. Globally, one observes an inverse relationship between the standard deviation and the mean porosity. This relationship is known as a regressive effect or proportional effect (David, 1988; Manchuk et al., 2009) and can be explained because the distribution of ELAN porosity is negatively skewed (Fig. 3). The standard deviation of ELAN porosity also turns out to be greater in the eastern part of the interwell region, indicating that the regressive effect is not uniform in this region (it actually depends on the Gaussian anamorphosis function, which varies with the east coordinate according to Eq. (4)). Accordingly, if an additional well could be drilled in the interwell region, it should better be placed between coordinates 250–350 m, where uncertainty in ELAN porosity is greater, rather than in the middle of the interwell region.

As for the individual realizations in Fig. 10, the mean ELAN porosity and the probability maps suggest the existence of one low-porosity structure and two to three high-porosity structures between the two

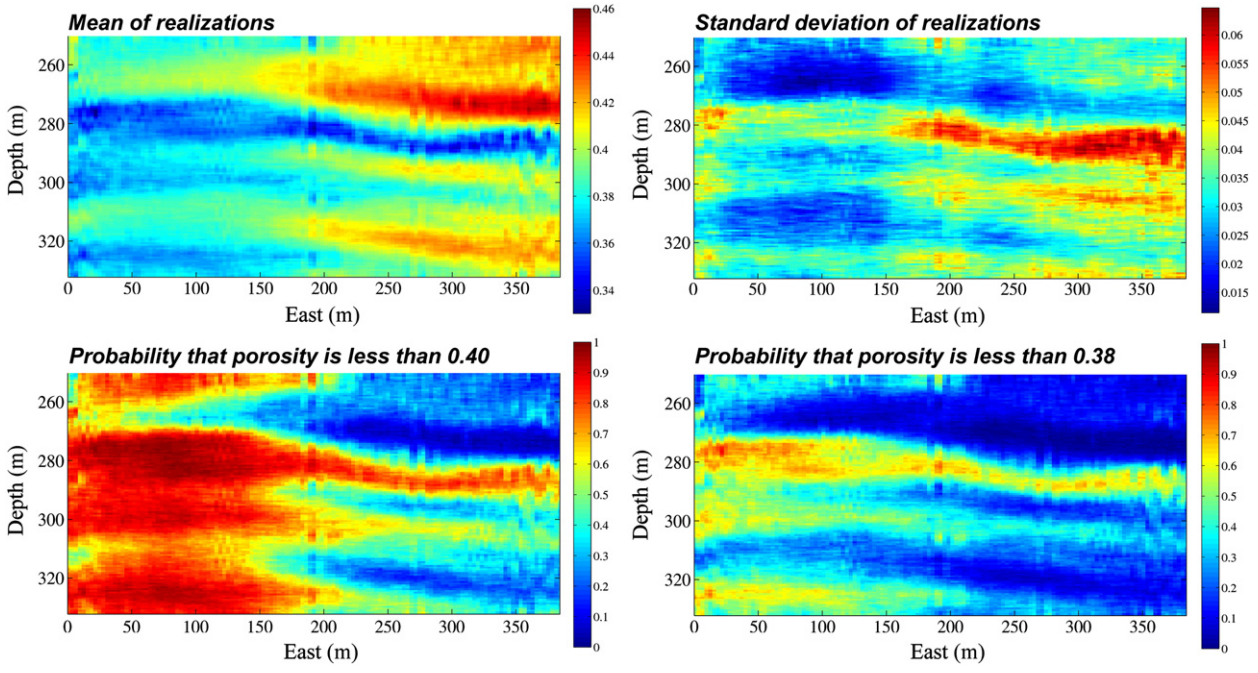

Fig. 11. Top: mean and standard deviation of ELAN porosity realizations. Bottom: probability that ELAN porosity is less than 0.40 or 0.38, estimated from 400 conditional realizations.

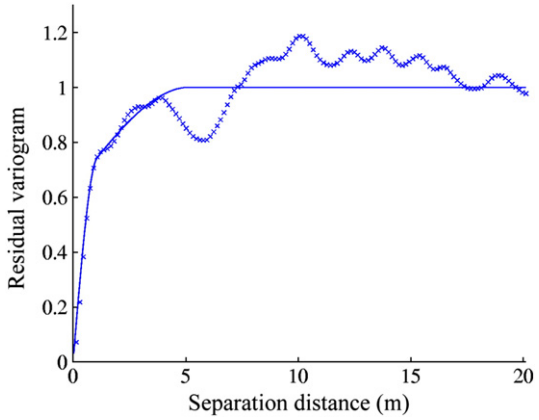

Fig. 13. Experimental residual variogram calculated along the vertical direction (crosses) and fitted isotropic model (solid line).

wells. This is corroborated by water well observations at the aquifer, as water production is very high in the zones above and below the identified low-porosity structure (Bennett and Recrenwald, 2002). In order to assess whether or not these structures effectively connect the two wells, the following exercise can be done:

1) Define a porosity threshold p.
2) For each realization of ELAN porosity
   a. Select the grid nodes for which the simulated porosity is greater than p.
   b. Determine if, among the selected grid nodes, there exists a structure (i.e., a set of contiguous nodes) that connects the two wells.
3) Calculate the number of realizations for which a structure has been identified, relative to the total number of realizations, as an estimate of the probability that the two wells are connected by a structure with porosity greater than p.
4) Repeat the same exercise for identifying low-porosity structures (at step 2a, select the grid nodes with simulated porosity less than threshold p).

The results of the exercise are indicated in Fig. 12, for porosity thresholds varying from 0.33 to 0.43. The increasing curve represents the probability (ordinate axis) that a structure with ELAN porosity lower than the threshold (abscissa axis) connects the two wells, while the decreasing curve represents the probability that a structure with ELAN porosity greater than the threshold connects the two wells. For instance, the increasing curve indicates that there is 23% probability that the two wells are connected by a structure with ELAN porosity less than 0.37, and that the probability increases to more than 50% if the porosity threshold is set to 0.38.

3.4. Simulation of ELAN porosity with a simplistic model

The realizations in Fig. 10 can be compared to the ones that would be obtained with a more simplistic model, consisting in splitting the ELAN porosity field into two components: on the one hand, a drift (trend) linearly related to P-wave impedance; on the other hand, a zero-mean residual that is independent of the drift. By assuming that the residual is the transform of a stationary Gaussian random field, the simulation of ELAN porosity can be achieved through the following steps:

1) Based on the well data, fit a linear regression model of ELAN porosity as a function of P-wave impedance.
2) Transform the values of the regression residual into normally distributed data.
3) Calculate the experimental variogram of the transformed residual and fit a theoretical model. In practice, the experimental variogram is known only along the vertical direction, so that an isotropic variogram is fitted (Fig. 13), supposing that the drift accounts for the anisotropy in the spatial distribution of ELAN porosity.
4) Simulate the residual in the interwell region.
5) Add the drift component and the simulated residual to obtain a realization of ELAN porosity.

As an illustration, Fig. 14 presents the maps of three realizations obtained through the previous steps, and a map of the drift component, which coincides with the mean of an infinitely large number of realizations since the residual has a zero mean. Although the latter map suggests the existence of structures of high and low porosity, these structures appear as more scattered and less connected than with the

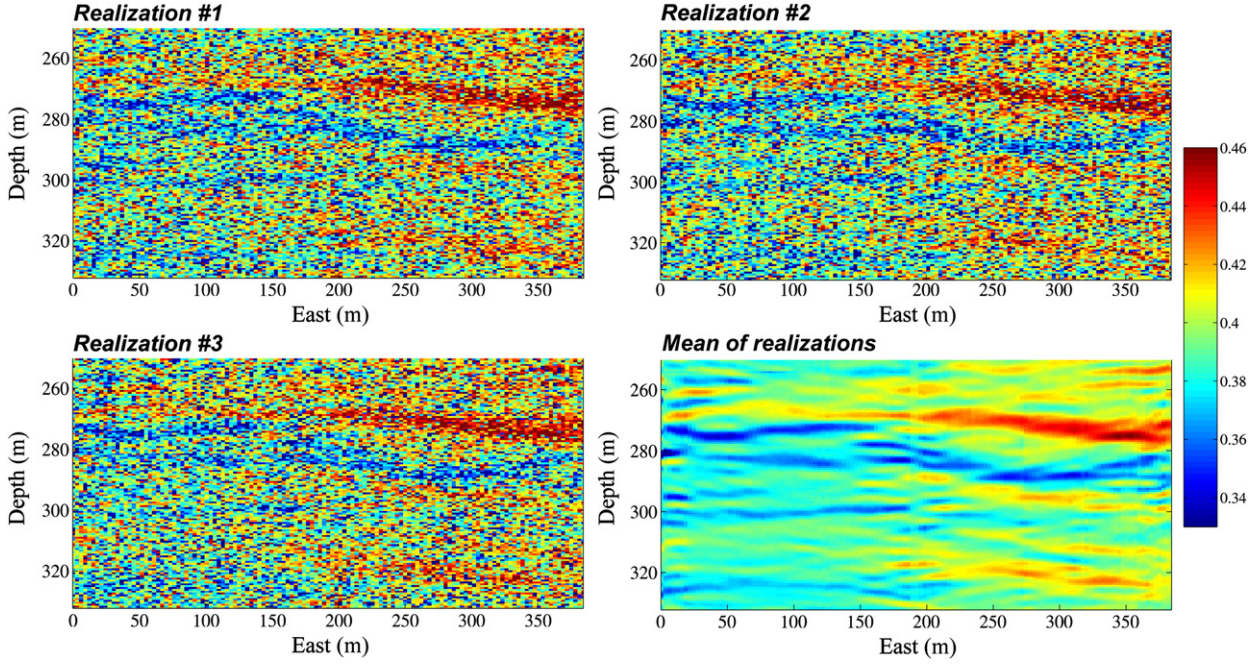

Fig. 14. Maps of three conditional realizations of ELAN porosity and of the drift component, equal to the mean of infinitely many realizations (simplistic model).

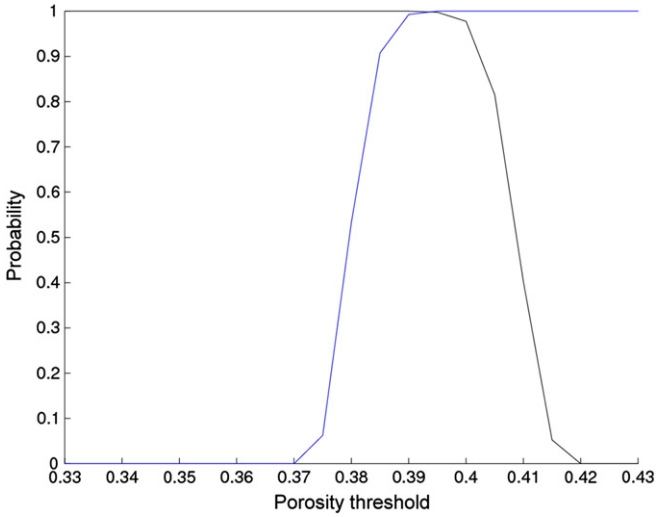

Fig. 15. Probability that a high-porosity structure (decreasing curve) or that a low-porosity structure (increasing curve) connects the two wells (simplistic model).

model developed in Section 2. This can be explained because the residual variogram (Fig. 13) is composed of two nested structures with a small range (1.1 m and 5.2 m, respectively), producing small-scale variability in the simulated residual and porosity values. This impression is confirmed when calculating the probability curves as defined in Fig. 12: the probability that the two wells are connected by a structure with ELAN porosity less than 0.37 is now very close to zero (Fig. 15). This disagrees with the water well observations and with the existence of a permeability barrier between the two wells.

4. Conclusions

While spatial prediction techniques such as cokriging provide a single, smoothed, model of subsurface properties, stochastic simulation enables the construction of multiple images (realizations) that are consistent with the available data and reproduce the true underlying spatial variability and small-scale heterogeneities.

In this paper, we focused on the simulation of porosity, which plays an important role in groundwater flow and helps to predict fluid paths in the aquifer at the well scale, based on porosity logs at two wells and high-resolution crosswell seismic measurements of P-wave impedance. To this end, a joint model of porosity and impedance has been elaborated and carefully checked against the available data in order to corroborate the successive model assumptions. Multiple realizations of porosity have been constructed and conditioned to the impedance data in the interwell region, giving a representation of our uncertainty in the true distribution of porosity. The set of realizations allow identifying one low-porosity structure acting as a permeability barrier in the depth interval between 270 m and 300 m, as well as two to three flow units above and below this structure, which are likely to connect the two wells. They also provide a visual assessment of the fluid path in the aquifer and suggest that the path in the lower flow units, formed by a network of heterogeneous conduits, is not as smooth as in the upper flow unit.

The fitting of the model is essential to assessing the connectivity of porosity structures. As an illustration, a simpler, but less realistic, model based on a decomposition of the porosity field into a drift and a residual component, shows much less connected structures than the proposed model.

Acknowledgments

This research was funded by the Chilean Commission for Scientific and Technological Research through CONICYT/FONDECYT/REGULAR/N°1130085 Project. The South Florida Water Management District provided the Florida aquifer data.

References

Belina, F.A., Ernest, J.R., Hollinger, K., 2009. Inversion of crosshole seismic data in heterogeneous environments: comparison of waveform and ray-based approaches. J. Appl. Geophys. 68, 85–94.
Bennett, M.W., Recrenwald, E.E., 2002. Hydrogeologic Investigation of the Floridian Aquifer System, Port Mayaca Site, Martin County. Preliminary Report, SFWMED, West Palm Beach, Florida.
Chilès, J.P., Delfiner, P., 2012. Geostatistics: Modeling Spatial Uncertainty, second ed. Wiley, New York.
Dafflon, B., Barrash, W., 2012. Three-dimensional stochastic estimation of porosity distribution: benefits of using ground-penetrating radar velocity tomograms in simulated-annealing-based or Bayesian sequential simulation approaches. Water Resour. Res. 48, W05553.
Dafflon, B., Irving, J., Hollinger, K., 2009. Simulated-annealing-based conditional simulation for local-scale characterization of heterogeneous aquifers. J. Appl. Geophys. 68, 60–70.
David, M., 1988. Handbook of Applied Advanced Geostatistical Ore Reserve Evaluation. Elsevier, Amsterdam.
De Fouquet, C., 1994. Reminders on the conditioning kriging. In: Armstrong, M., Dowd, P.A. (Eds.), Geostatistical Simulations. Kluwer Academic, Dordrecht, pp. 131–145.
Doyen, P.M., 1988. Porosity from seismic data: a geostatistical approach. Geophysics 53 (10), 1263–1276.
Dubreuil-Boisclair, C., Gloaguen, E., Marcotte, D., Giroux, B., 2011. Heterogeneous aquifer characterization from ground-penetrating radar tomography and borehole hydrogeophysical data using nonlinear Bayesian simulations. Geophysics 76 (4), 1–13.
Dubrule, O., 2003. Geostatistics for Seismic Data Integration in Earth Models. Society of Exploration Geophysicists.
Emery, X., 2005. Variograms of order ω: a tool to validate a bivariate distribution model. Math. Geol. 37 (2), 163–181.
Emery, X., 2008. A turning bands program for conditional co-simulation of cross-correlated Gaussian random fields. Comput. Geosci. 34 (12), 1850–1862.
Emery, X., 2010. Iterative algorithms for fitting a linear model of coregionalization. Comput. Geosci. 36 (9), 1150–1160.
Emery, X., 2012. Cokriging random fields with means related by known linear combinations. Comput. Geosci. 38 (1), 136–144.
Ikelle, L.T., Amundsen, L., 2005. Introduction to Petroleum Seismology. Society of Exploration Geophysicists, Tulsa.
Jennings Jr., J.W., Ruppel, S.C., Ward, W.B., 2000. Geostatistical analysis of permeability data and modeling of fluid-flow effect in carbonate outcrops. Society of Petroleum Engineering (SPEREE). 292 (August).
Kazatchenko, E., Markov, M., Mousatov, A., Parra, J.O., 2006. Carbonate microstructure determination by inversion of acoustic and electrical data: application to a south Florida aquifer. J. Appl. Geophys. 59, 1–15.
Kerans, C., Lucia, F.J., Senger, R.K., 1994. Integrated characterization of carbonate ramp reservoir using Permian San Andres formation outcrops analogs. AAPG Bull. 78, 181.
Malehmir, A., Durrheim, R., Bellefleur, G., Urosevic, M., Juhlin, C., White, D.J., Milkereit, B., Campbell, G., 2012. Seismic methods in mineral exploration and mine planning: a general overview of past and present case histories and a look into the future. Geophysics 77 (5), WC173–WC190.
Manchuk, J.G., Leuangthong, O., Deutsch, C.V., 2009. The proportional effect. Math. Geosci. 41 (7), 799–816.
Matheron, G., 1989. The internal consistency of models in Geostatistics. In: Armstrong, M. (Ed.), Geostatistics. Kluwer Academic, Dordrecht, pp. 21–38.
Parra, J., Emery, X., 2013. Geostatistic applied to crosswell reflection seismic for imaging carbonate aquifers. J. Appl. Geophys. 92, 68–75.
Parra, J.O., Hackert, C.L., Bennett, W.M., 2006. Permeability and porosity images based on P-wave surface seismic data: application to a South Florida aquifer. Water Resour. Res. 42 (2), 591 (W02415).
Parra, J.O., Hackert, C.L., Richardson, E., Clayton, N., 2009. Porosity and permeability images based on crosswell seismic measurements integrated with FMI logs at the Port Mayaca aquifer, South Florida. Lead. Edge 28, 1212–1219.
Rivoirard, J., 1994. Introduction to Disjunctive Kriging and Nonlinear Geostatistics. Oxford University Press, Oxford.
Wackernagel, H., 2003. Multivariate Geostatistics — An Introduction with Applications, third ed. Springer, Berlin.